

## Feldspar Raman shift and application as a magmatic thermobarometer

KENNETH S. BEFUS<sup>1,\*†</sup>, JUNG-FU LIN<sup>2</sup>, MIGUEL CISNEROS<sup>2</sup>, AND SUYU FU<sup>2</sup>

<sup>1</sup>Department of Geosciences, Baylor University, Waco, Texas 76798, U.S.A.

<sup>2</sup>Department of Geological Sciences, Jackson School of Geosciences, University of Texas at Austin, Austin, Texas 78712, U.S.A.

### ABSTRACT

We calibrate the pressure-dependent Raman shift of feldspars by measuring spectra of 9 compositionally diverse plagioclase and alkali feldspars at pressures ranging between 0.1 MPa and 3.6 GPa using a diamond-anvil cell coupled with Raman spectroscopy. We observe up to 12 vibrational modes that are caused by deformation of Si(Al)O<sub>4</sub> tetrahedral chains. The most intense modes are  $\nu_{22}$ ,  $\nu_{24}$ , and  $\nu_{25}$ , which are produced by stretching and bending of four-membered Si(Al)-O-Si(Al) rings. Because modes are a product of lattice environments, feldspar composition may relate to mode frequency. We find that the frequencies of the  $\nu_{25}$  mode correlates with composition, whereas the other intense bands do not correlate with composition. All feldspar compositions exhibit modes that shift linearly ( $r^2 > 0.9$ ) to higher frequencies with increasing pressure. Modes  $\nu_{22}$ ,  $\nu_{24}$ , and  $\nu_{25}$  shift to higher frequencies with slopes that range from  $1.7 \pm 0.5$  to  $5.5 \pm 1.6$  cm<sup>-1</sup> GPa<sup>-1</sup>, and provide the best combination of intensity and pressure-sensitivity. For all compositions the  $\nu_{22}$  mode exhibits the most advantageous pressure-dependent ( $P$ - $T$ ) frequency shift. We use an elastic model, thermodynamic properties, and shear moduli to establish the pressure-temperature dependent sensitivity of feldspar inclusions hosted by garnet, clinopyroxene, and olivine. Raman shifts for all feldspars are  $< 2$  cm<sup>-1</sup> for crustal and upper lithosphere conditions. Albitic plagioclase inclusions show the least temperature-sensitive inclusion pressures and provide the best barometers, followed by alkali feldspars and anorthitic plagioclase. Our new calibration allows Raman spectroscopy of feldspars to be used to quantify  $P$ - $T$  conditions for crustal magmatic rocks, low- to high-grade metamorphic rocks, and the mantle.

**Keywords:** Raman, barometry, inclusions, magma storage; Rates and Depths of Magma Ascent on Earth

### INTRODUCTION

The temperature and pressure conditions of magmas are important variables that exert control over the evolution and eruptive behavior of volcanic systems. Temperature conditions for many magmatic systems can be inferred using major and trace element compositions of minerals (e.g., Watson et al. 2006; Thomas et al. 2010; Waters and Lange 2015). The pressures and storage depths of magmas are less readily constrained. Dissolved volatile contents of melt inclusions provide one method for estimating magmatic pressures, but they have limitations caused by leaking and saturation assumptions (e.g., Lowenstern 1995; Wallace et al. 1999; Gaetani et al. 2012).

In recent years, petrologists have implemented Raman spectroscopy of solid inclusions as a reliable tool for constraining pressure-temperature ( $P$ - $T$ ) conditions of host mineral growth (e.g., Sobolev et al. 2000; Guiraud and Powell 2006; Kohn 2014; Ashley et al. 2014a, 2014b, 2015a, 2015b; Angel et al. 2015; Zhukov and Korsakov 2015). Raman spectroscopy measures the inelastic scattering of incident light by lattice vibrations in the sample producing Raman spectra that represent specific Raman active vibrational modes; herein referred to as bands. The shape

and position of each individual band corresponds to different bonding, crystallographic symmetry, and atomic environments (Nasdala et al. 2004). As a result, every mineral has a unique spectral fingerprint. Crystal lattice compression or expansion in response to changing pressure and temperature conditions will produce  $P$ - $T$  dependent Raman frequency shifts that can be calibrated for individual minerals and used as secondary thermobarometry.

Before Raman spectra can be used for thermobarometry, it is critical to first establish the target mineral's vibrational characteristics including band position and subsequent pressure dependence. Pressure estimates from compressible mineral inclusions can then be extracted because rigid, relatively incompressible host crystals preserve residual pressures related to inclusion entrapment (Guiraud and Powell 2006; Kohn 2014; Angel et al. 2017). Entrapment conditions are estimated by comparing the spectral shift of Raman bands in the inclusion under entrapment pressure and the same phase at ambient conditions. The measured Raman shift establishes the current, elevated pressure of the inclusion at ambient temperature. The current pressure of the inclusion is related to—but not equal to—entrapment pressure, which instead is a function of current inclusion pressure and the thermal expansivity and compressibility of host and inclusion during exhumation (mantle and metamorphic), ascent (magmatic), and cooling (Fig. 1) (Guiraud and Powell 2006;

\* E-mail: Kenneth\_Befus@Baylor.edu

† Special collection papers can be found online at <http://www.minsocam.org/MSA/AmMin/special-collections.html>.

Kohn 2014). The resulting decompression and cooling of the inclusion-host pair results in volume changes. The thermodynamic properties of expansivity and incompressibility are well characterized for many rock-forming minerals so the precise volumetric changes can be quantified for any given set of entrapment conditions (e.g., Berman 1988; Holland and Powell 2011). Inclusion entrapment conditions can be calculated by using a 1D isotropic elastic model:

$$\frac{V_h(P_i, T)}{V_h(P_o, T_o)} = \frac{V_i(P_i, T)}{V_i(P_o, T_o)} - \frac{3}{4}G(P_i - P) \quad (1)$$

where  $V_h(P, T)$  is the volume of the host crystal at current conditions,  $V_h(P_o, T_o)$  is the volume of the host crystal at entrapment conditions,  $V_i(P, T)$  is the volume of the inclusion at current conditions,  $V_i(P_o, T_o)$  is the volume of the inclusion at entrapment conditions,  $P_i$  is current inclusion pressure,  $P$  is ambient pressure, and  $G$  is the shear modulus of the host (see Guiraud and Powell 2006; Kohn 2014 for in depth discussion). The equation is itera-

tively solved by changing the volume of inclusion-host pairs and entrapment pressure until both sides of the equation are equal.

Although the method above is straightforward and has been used in impactful studies of both mantle and metamorphic systems, Raman thermobarometry for magmatic systems remains uncalibrated and untested. In this study, we measured the Raman spectra for a suite of 9 compositionally diverse feldspars in the orthoclase-albite-anorthite system. Feldspars present an excellent target because they comprise ~60% of the crust, they are highly compressible, and are geologically stable in igneous, metamorphic, and mantle rocks at pressures less than 3 GPa (Holland 1980; Angel 1994; Rudnick and Fountain 1995; Daniel et al. 1997; Deer et al. 2001; Benusa et al. 2005). For this reason, the elastic properties of feldspars have been rigorously examined for the past four decades, including some studies of the Raman spectra of feldspars (e.g., Mernagh 1991; Angel 2004; Benusa et al. 2005; Freeman et al. 2008; Aliatis et al. 2017). We build upon past work by collecting spectra at ambient conditions and at increments of increased pressure ranging up to 3.6 GPa. We find that all feldspars produce prominent Raman bands, and those bands linearly shift to higher wavenumbers with increasing pressures. We then couple our new empirical results with thermodynamic considerations (Eq. 1) to produce the first Raman thermobarometry calibrations for magmatic systems. Because feldspars are a major constituent of many rock types, our study also greatly expands Raman thermobarometry applications for mantle and metamorphic environments.

## METHODS

We chose nine feldspars for high-pressure Raman analyses from collections at the Department of Mineral Sciences, Smithsonian Institution, and at Baylor University. Samples were chosen to ensure that Raman spectra were investigated for structures and compositions spanning the feldspar ternary (Table 1). To confirm a wide range was selected, major-element compositions of the targeted feldspars were analyzed by using a JEOL JXA-8200 electron microprobe at the University of Texas at Austin (Table 1). Operating conditions employed a 10 nA beam current with a 15 keV accelerating voltage. The beam was defocused to 2  $\mu$ m diameter and Na migration was corrected by using the time-dependent intensity corrections on Probe for Windows. We analyzed working standards throughout the session to monitor analytical quality and instrumental drift.

Raman spectra of the feldspars were measured using a confocal Renishaw inVia

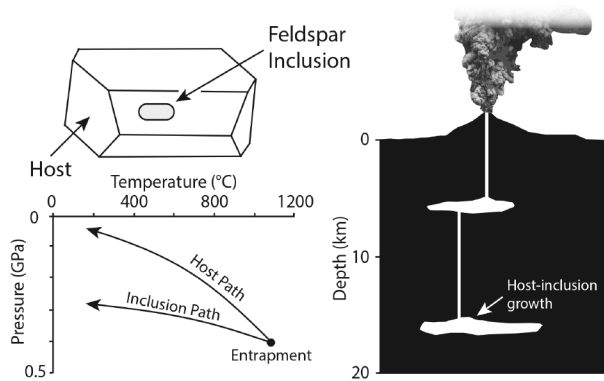


**FIGURE 1.** Schematic  $P$ - $T$  pathway of inclusion-host pair during cooling and ascent from magmatic storage conditions. The inclusion may remain overpressured because it remains confined by the host during ascent (modified from Guiraud and Powell 2006).

**TABLE 1.** Compositions of feldspars

Feldspar	Location	SiO <sub>2</sub>	Al <sub>2</sub> O <sub>3</sub>	FeO <sup>a</sup>	MgO	CaO	K <sub>2</sub> O	Na <sub>2</sub> O	Total	Or	Ab	An	<i>n</i>
Sanidine	Mesa Falls Tuff, WY	65.79	18.91	0.11	0.01	0.34	10.12	4.17	99.4	60.4	37.9	1.7	10
		(0.58)	(0.19)	(0.04)	(0.01)	(0.03)	(0.12)	(0.23)	(0.72)	(1.3)	(1.5)	(0.1)	
Sanidine (less K)	Solfatara Plateau, WY	66.69	18.92	0.14	0.01	0.53	8.89	5.34	99.81	48.9	48.5	2.7	28
		(0.59)	(0.22)	(0.02)	(0.01)	(0.04)	(0.56)	(0.37)	(0.80)	(3.3)	(3.3)	(0.2)	
Anorthoclase	Erebus, Antarctica	63.02	21.87	0.20	0.01	3.03	3.38	7.28	98.79	19.9	65.1	15.0	10
		(0.58)	(0.41)	(0.08)	(0.01)	(0.30)	(0.27)	(0.22)	(0.71)	(1.6)	(1.7)	(0.5)	
Albite <sup>b</sup>	Amelia Granite, VA	69.25	20.17	0.02	0.01	0.03	0.18	11.76	101.42	1.0	98.9	0	8
		(0.39)	(0.18)	(0.02)	(0.01)	(0.01)	(0.04)	(0.34)	(0.61)	(0.2)	(0.2)		
Oligoclase	Dome 25, Mono Craters, CA	63.57	22.08	-	-	3.84	1.11	8.94	99.54	6.2	75.8	18.0	10
		(0.57)	(0.29)			(0.25)	(0.08)	(0.24)	(0.51)	(0.5)	(0.9)	(1.2)	
Oligo-andesine	Unknown, teaching collection	62.32	24.02	-	0.01	5.80	1.52	7.20	100.86	8.8	63.1	28.1	8
		(1.84)	(1.18)		(0.01)	(1.08)	(0.53)	(0.31)	(0.71)	(3.1)	(2.4)	(5.3)	
Andesine <sup>b</sup>	Toba Tuff, Indonesia	56.85	26.97	0.19	0.01	8.97	0.52	6.08	99.48	3.0	53.4	43.6 (7.2)	19
		(1.86)	(1.23)	(0.06)	(0.01)	(1.48)	(0.14)	(0.74)	(0.94)	(0.8)	(6.4)		
Labradorite	Unknown, teaching collection	53.85	28.71	0.21	0.01	11.53	0.32	4.69	99.31	1.8	41.6	56.5 (0.7)	10
		(0.34)	(0.18)	(0.03)	(0.01)	(0.08)	(0.05)	(0.13)	(0.44)	(0.1)	(0.7)		
Anorthite	Unknown, teaching collection	44.84	35.91	0.45	0.11	19.55	0.01	0.55	101.41	0	4.8	95.1 (0.1)	10
		(0.37)	(0.16)	(0.06)	(0.01)	(0.12)	(0.01)	(0.07)	(0.31)		(0.1)		

Note: Analyses by electron microprobe. Major oxides reported in weight percent and are averages of *n* samples. Values in parentheses represent standard deviation.

<sup>a</sup> Total iron reported as FeO, not measured in all specimens.

<sup>b</sup> Albite and andesine are from Smithsonian Institution and are samples NMNH 116398-15A and 88280-89, respectively.

Raman Microscope in the Mineral Physics Laboratory at the University of Texas at Austin (e.g., Lin et al. 2012). We used the 532 nm wavelength and laser power ranging up to 10 mW. The system has a focused beam size of  $\sim 1 \mu\text{m}$  and a spectral pixel resolution of  $0.9 \text{ cm}^{-1}$ , and a practical resolution  $< 1.5 \text{ cm}^{-1}$ . Prior to analyses, 10–40  $\mu\text{m}$  diameter cleavage fragments of the targeted feldspar crystals were loaded into a diamond-anvil cell (DAC). In all analyses we focused the beam on the surface of the clear cleavage fragment. Deionized water, ethanol, and a synthetic ruby sphere were also loaded into the DAC, which were used as the pressure medium and pressure calibrant, respectively (e.g., Mao et al. 1986; Dewale et al. 2008). Uncertainty on the ruby pressure calibration is  $\pm 30 \text{ MPa}$  based on reproducibility and the spectral resolution of the Raman system. A silicon standard was used to calibrate the Raman system for absolute wavenumber from the elastic peak. We used a least squares, smoothing interpolant function to fit and measure all spectra. Raman spectra were first collected at ambient pressure conditions. Pressure was then increased within the DAC in small increments. We sought to generate small, regular pressure increments to fully replicate pressure conditions in the crust, but were somewhat limited by the sensitivity of the hex screws that were tightened manually. All analyses were performed at room temperature ( $\sim 25^\circ\text{C}$ ).

We collected Raman spectra in three experiments over a spectral range of  $\sim 100$  to  $1200 \text{ cm}^{-1}$ . Diamond Raman bands from the DAC occur at  $\sim 1330$  and between  $2100$ – $2700 \text{ cm}^{-1}$  (Solin and Ramdas 1970; Prawer and Nemanich 2004), Raman bands from ethanol used in the pressurizing medium in the first experiment produced prominent bands at  $\sim 880$ ,  $\sim 1030$ , and  $\sim 1090 \text{ cm}^{-1}$  (Mammone and Sharma 1980). In all cases, diamond and ethanol bands do not obscure feldspar bands. In the first experiment we analyzed albite ( $\text{Or}_1\text{Ab}_{99}\text{An}_0$ ), andesine ( $\text{Or}_7\text{Ab}_{53}\text{An}_{44}$ ), anorthoclase ( $\text{Or}_{20}\text{Ab}_{65}\text{An}_{15}$ ), and labradorite ( $\text{Or}_2\text{Ab}_{42}\text{An}_{57}$ ) at 13 increments from ambient pressure to 3.6 GPa. Individual pressure increments ranged from 50 to 710 MPa, and averaged 300 MPa (3.0 kb). In the second experiment we analyzed anorthite ( $\text{Or}_0\text{Ab}_5\text{An}_{95}$ ) and sanidine ( $\text{Or}_{60}\text{Ab}_{38}\text{An}_2$ ) in 12 increments ranging from ambient pressure up to 3.0 GPa. Pressure increments in that experiment ranged from 100 to 830 MPa, and averaged 260 MPa (2.6 kb). In the third experiment we analyzed sanidine ( $\text{Or}_{49}\text{Ab}_{49}\text{An}_2$ , less potassic than sanidine in the first experiment), oligoclase ( $\text{Or}_8\text{Ab}_{76}\text{An}_{18}$ ), and oligo-andesine (sits on the ternary join at  $\text{Or}_9\text{Ab}_{63}\text{An}_{28}$ ) in 14 increments ranging up to 3.5 GPa. Increments ranged from 40 to 680 MPa, and averaged 250 MPa. Fewer bands were identified in feldspars analyzed during the second and third experiments. The maximum pressure in both experiments was chosen to correspond to the pressure stability of feldspars (Holland 1980; Angel 1994; Deer et al. 2001; Benusa et al. 2005; Holland and Powell 2011).

Raman band positions and shapes are sensitive to many aspects of the atomic environment of minerals, including bonding, ions, and symmetry (Geiger and Kolesov 2002). Because the lattice environments of feldspars are largely similar, spectra of feldspar structures should be qualitatively consistent across all feldspar compositions (McKeown 2005; Freeman et al. 2008). All of the feldspar specimens are magmatic. Albite and anorthite are from intrusive rocks, with the remaining seven feldspars from rapidly quenched volcanic samples, and thus likely preserve high-temperature disorder. We have also carefully examined each sample with a petrographic microscope and using e-beam techniques. Neither exsolution nor textural heterogeneities are observed in any specimen using these analyses.

Band intensity is a subjective criterion that varies with crystallographic orientation relative to the incident light (Nasdala et al. 2004). In some orientations bands will disappear (become Raman inactive) because the polarized incident beam of light is unable to produce vibrations in that crystallographic direction (e.g., Nasdala et al. 2004; Mernagh 1991; Frogner et al. 1998; Aliatis et al. 2015). In our study, sharp, clean feldspar cleavage fragments rested on the surface of the DAC, perpendicular to the incident laser. Our experimental geometry ensured crystallographic axes of the low-symmetry, triclinic and monoclinic feldspars did not align with the incident light and thus vibrations were Raman-active.

We identify Raman bands as vibrational modes produced by flexing of the  $\text{Si}(\text{Al})\text{O}_4$  tetrahedral chains that comprise the crankshaft structure, following the excellent treatments in past studies (e.g., Geiger and Kolesov 2002; Benusa et al. 2005; Nasdala et al. 2004; McKeown 2005; Freeman et al. 2008; Aliatis et al. 2015, 2017). Throughout, we identify modes listed sequentially from  $\nu_1$  to  $\nu_{39}$  per band frequency after Aliatis et al. (2015) as that study has provided extensive insights into the vibrational characteristics of the Raman modes of feldspars. We maintain consistency with this approach across all feldspar structures and compositions.

Individual modes can be classified into groups that are related to frequency range, intensity, and vibration environment (e.g., Freeman et al. 2008). Group I modes are categorized as  $\nu_1$  to  $\nu_{25}$ ; they are the most intense and have frequencies between 450 and  $580 \text{ cm}^{-1}$ . Group I modes are produced by stretching, bending, and “breathing” of four-membered rings of  $\text{Si}(\text{Al})\text{-O-Si}(\text{Al})$  (e.g., Sharma et al. 1983; Mernagh 1991; McKeown 2005; Freeman, et al. 2008; Aliatis et al. 2015). One of

the most intense modes in all feldspars is  $\nu_{24}$ , which occurs near  $\sim 510 \text{ cm}^{-1}$ . Group II ( $\nu_{11}$  to  $\nu_{20}$ ) and Group III ( $\nu_1$  to  $\nu_{10}$ ) modes occur from 200 to 450 and  $< 200 \text{ cm}^{-1}$ , respectively. Modes in Group II and III are attributed to both rotation-translation of  $\text{SiO}_4$  tetrahedra and to external bending of alkali cations (Frogner, et al. 1998; Geiger and Kolesov 2002; McKeown 2005; Aliatis et al. 2015).

Group IV modes ( $\nu_{26}$ – $\nu_{31}$ ) have frequencies between 600 to  $800 \text{ cm}^{-1}$ . These modes are attributed to internal  $\text{Si-O}$  tetrahedra deformation, and may differ with the presence of Al, Na, Ca, and K in the structure. Alkalis have higher coordination and weaker bonding than  $\text{SiO}_4$  tetrahedrons, which causes their vibrations to occur at lower energies. In some feldspars (especially alkali feldspars like sanidine and anorthoclase), band intensities above  $600 \text{ cm}^{-1}$  become less intense in response to disordered  $\text{Si/Al}$  distributions that produces broader, weaker peaks (Mernagh 1991; Velde and Boyer 1985; Freeman et al. 2008). Group V modes ( $\nu_{32}$  to  $\nu_{39}$ ) occur between 900– $1200 \text{ cm}^{-1}$  and are caused by  $\text{Si}(\text{Al})\text{-O}$  stretch vibrations and breathing (McKeown 2005; Freeman et al. 2008; Aliatis et al. 2015). For more information, we point the reader to the following articles for focused discussions on the Raman spectra for specific feldspars including albite (Frogner et al. 1998; McKeown 2005; Aliatis et al. 2017), anorthite (Sharma et al. 1983; Matson et al. 1986), and sanidine (Velde and Boyer 1985; Matson et al. 1986).

## RESULTS

Each of the analyzed feldspars produced distinct modes with intensities above background (Fig. 2). Past studies of Raman spectra for diverse feldspar compositions corroborate the posi-

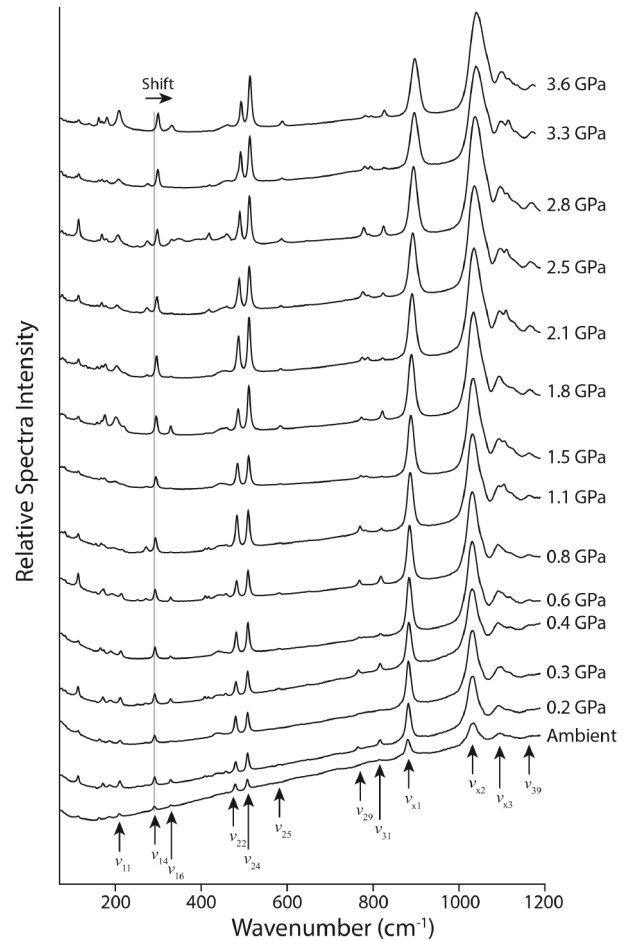


FIGURE 2. Raman spectra of albite with increasing pressure. Modes are labeled with arrows. Gray line highlights shift with increasing pressure for  $\nu_{14}$ , the  $291 \text{ cm}^{-1}$  band.

tions and intensities of our new results (Mernagh 1991; Frogner et al. 1998; McKeown 2005; Freeman et al. 2008; Aliatis et al. 2015, 2017). To build on past research, we first establish mode frequencies at ambient conditions. We then demonstrate that modes shift linearly to sequentially higher wavenumber at higher pressures (Fig. 3; Supplemental<sup>1</sup> Table 1). Most of the modes with measurable intensities at ambient pressure maintained detectable intensities as pressure increased. Some modes lost

intensity relative to background and ultimately could no longer be resolved with confidence.

### Raman frequency shift with pressure

Over the range of pressures examined, albite ( $\text{Or}_1\text{Ab}_{99}\text{An}_0$ ) produces 12 distinct modes (Supplemental<sup>1</sup> Table 1). At ambient pressures we observe  $\nu_7$ ,  $\nu_{10}$ ,  $\nu_{11}$ ,  $\nu_{14}$ ,  $\nu_{16}$ ,  $\nu_{22}$ ,  $\nu_{24}$ , and  $\nu_{31}$  (Fig. 2). Modes  $\nu_8$ ,  $\nu_{25}$ ,  $\nu_{29}$ , and  $\nu_{39}$  are not observed at ambient pressures,

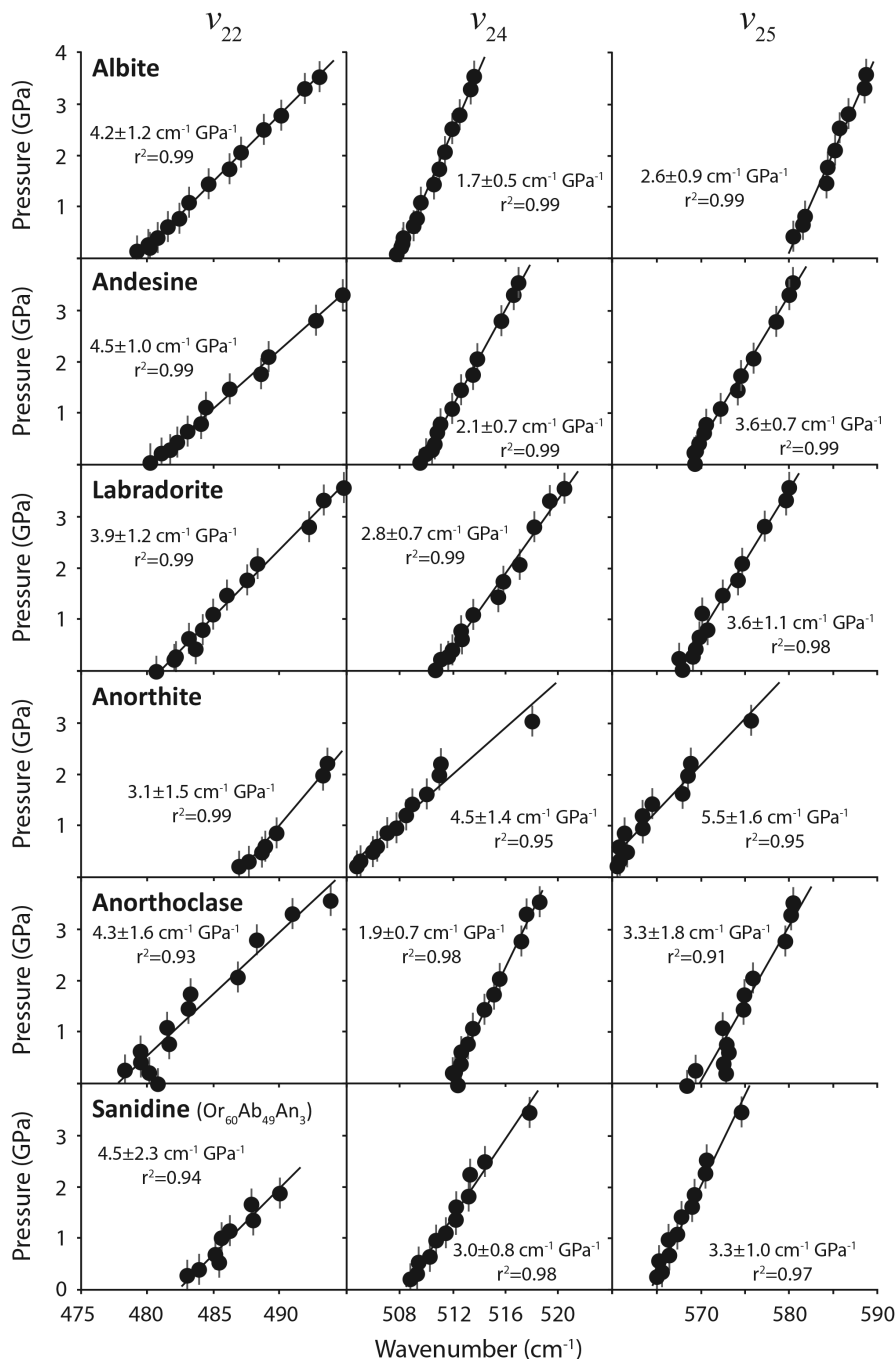


**FIGURE 3.** Linear shift with increasing pressure of  $\nu_{22}$ ,  $\nu_{24}$ , and  $\nu_{25}$  for feldspar compositions. Data are presented in Supplemental<sup>1</sup> Table 1. Pressure uncertainty from diamond-anvil cells are shown as vertical bars. Wavenumber uncertainty is smaller than symbol size.

but are resolvable at higher pressures. At all pressures  $\nu_{22}$  and  $\nu_{24}$  have the highest intensities. We attribute the intermittent occurrence of some modes to low intensities. Each mode linearly shifts to higher wavenumber with increasing pressure, but does so at different rates (Supplemental<sup>1</sup> Table 1). Only  $\nu_{16}$  displays a poor fit to a linear shift ( $r^2 = 0.8$ ), all remaining modes shift with  $r^2 > 0.97$ . The shifts of the most intense  $\nu_{22}$  and  $\nu_{24}$  are  $4.2 \pm 1.2$  and  $1.7 \pm 0.5 \text{ cm}^{-1} \text{ GPa}^{-1}$ , respectively, and each has an  $r^2 > 0.99$  (Fig. 3).

We observe 5 distinct modes in oligoclase ( $\text{Or}_6\text{Ab}_{76}\text{An}_{18}$ ), and each shifts to higher wavenumber with increasing pressure with  $r^2$  values  $> 0.9$ . Mode  $\nu_{24}$  is the most intense at all pressures, followed by  $\nu_{22}$  as the second most intense. The  $\nu_{14}$ ,  $\nu_{19}$ , and  $\nu_{25}$  modes lose intensity with increasing pressure until they finally become irresolvable near 2 GPa.

Oligo-andesine ( $\text{Or}_9\text{Ab}_{63}\text{An}_{28}$ ) produced the spectra with the least intense bands. We were able to only identify 3 distinct modes at  $\nu_{14}$  at  $287 \text{ cm}^{-1}$ ,  $\nu_{22}$  at  $475 \text{ cm}^{-1}$ , and  $\nu_{24}$  at  $515 \text{ cm}^{-1}$ . Mode  $\nu_{24}$  was present at all pressures ranging up to 3.5 GPa, and displays a systematic  $2.4 \pm 0.9 \text{ cm}^{-1} \text{ GPa}^{-1}$  linear shift to higher wavenumber with increasing pressure. Modes  $\nu_{14}$  and  $\nu_{22}$  show poor correlation between wavenumber and pressure, and they were not identifiable at pressures higher than 0.9 and 2.6 GPa, respectively.

Andesine ( $\text{Or}_3\text{Ab}_{53}\text{An}_{44}$ ) produces 11 distinct modes at ambient pressure (Supplemental<sup>1</sup> Table 1). At all pressures the  $\nu_{24}$  has the strongest intensities, followed by the  $\nu_{25}$  and  $\nu_{14}$  modes. The  $\nu_{19}$  mode has the weakest intensity and displays no correlation between wavenumber and pressure. All other modes show a positive, linear correlation between wavenumber and increasing pressure (Fig. 3).

We find that labradorite ( $\text{Or}_2\text{Ab}_{42}\text{An}_{57}$ ) has 11 modes, all of which display a linear shift to higher wavenumber with increasing pressure (Supplemental<sup>1</sup> Table 1). Modes  $\nu_{10}$  and  $\nu_{19}$  have the weakest intensities and were only intermittently identifiable. As with the other feldspars,  $\nu_{24}$  has the highest intensity, followed by  $\nu_{22}$ ,  $\nu_{14}$ , and  $\nu_{25}$ . All modes exhibit excellent linear shifts to higher wavenumber with increasing pressure (Fig. 3) ( $r^2 > 0.98$ ), with the exception of  $\nu_{14}$ , which correlates more poorly ( $r^2 = 0.78$ ).

Anorthite ( $\text{Or}_0\text{Ab}_5\text{An}_{95}$ ) produces 9 modes (Supplemental<sup>1</sup> Table 1). The  $\nu_{14}$ ,  $\nu_{18}$ , and  $\nu_{20}$  modes have faint intensities, and are sometimes not measureable. Those three modes also show a correlation between wavenumber position and increasing pressure, but the linear relationships have  $r^2 < 0.9$ . Each of the remaining modes displays clear linear shifts to higher wavenumbers with increasing pressure ( $r^2 > 0.95$ ).

We identify 10 modes in anorthoclase ( $\text{Or}_{20}\text{Ab}_{65}\text{An}_{15}$ ) (Supplemental<sup>1</sup> Table 1). In general, the anorthoclase modes are among the least intense of all the analyzed compositions, and show weaker correlation between wavenumber and increasing pressure. The majority of the modes have linear shifts with increasing pressure with  $r^2 > 0.9$ , but the two modes  $\nu_{10}$  and  $\nu_{14}$  correlate poorly ( $r^2 = 0.82$  and  $0.79$ , respectively).

Finally, we measured spectra of 2 sanidine specimens, which contain  $\sim 10$  mol% difference in Na and K. In the more potassic sanidine ( $\text{Or}_{60}\text{Ab}_{38}\text{An}_2$ ) we observe 5 modes;  $\nu_9$ ,  $\nu_{14}$ ,  $\nu_{22}$ ,  $\nu_{24}$ , and  $\nu_{25}$  (Supplemental<sup>1</sup> Table 1). All of the modes show linear correlations between frequency and increasing pressure. Modes  $\nu_9$

and  $\nu_{14}$  exhibit low intensities making them difficult to resolve. When present, they show the poorest correlation between wavenumber and pressure ( $r^2 = 0.84$  and  $0.74$ , respectively). At low pressure  $\nu_{22}$  is the second most intense, but counts diminish with increasing pressure until it is not found at pressures greater than 2 GPa. When present,  $\nu_{22}$  shifts linearly at  $4.5 \pm 2.3 \text{ cm}^{-1} \text{ GPa}^{-1}$ . Modes  $\nu_{24}$  and  $\nu_{25}$  are present at all pressures and they shift at  $3.0 \pm 0.8$  and  $3.3 \pm 1.0 \text{ cm}^{-1} \text{ GPa}^{-1}$ , respectively, and each has an  $r^2 > 0.97$ . The more sodic sanidine ( $\text{Or}_{49}\text{Ab}_{49}\text{An}_3$ ) produced only 3 modes at  $\nu_{14}$ ,  $\nu_{22}$ , and  $\nu_{24}$  (Supplemental<sup>1</sup> Table 1). Mode  $\nu_{24}$  is the most intense at all pressures and displays a strong correlation between increasing wavenumber and increasing pressure ( $r^2 = 0.96$  and slope of  $3.1 \pm 1.1 \text{ cm}^{-1} \text{ GPa}^{-1}$ ). Modes  $\nu_{14}$  and  $\nu_{22}$  similarly display positive correlation between wavenumber and pressure, with  $r^2$  values of 0.69 and 0.98, respectively.

### Raman frequency shift with composition

When we compare modes across the suite of feldspars we find that composition may be related to mode frequency (Fig. 4). Mode  $\nu_{24}$ , an intense band in each sample, displays a non-linear, cresting shift with feldspar composition (Fig. 4c). Frequency initially increases for  $\nu_{24}$  with increasing Na content from  $\text{Ab}_0$  to  $\sim \text{Ab}_{75}$ . The highest wavenumber is reached between  $\text{Ab}_{50}$  and  $\text{Ab}_{75}$ , which then decays to lower wavenumber. The  $\nu_{25}$  mode displays an excellent linear correlation between increasing wavenumber and increasing Ab content ( $r^2 = 0.98$ ) (Fig. 4d). The correlation with Ab content holds even when sanidine and anorthoclase are included, making it the only linear relationship that holds for all feldspar compositions.

## DISCUSSION

### Raman frequency shift with composition

Raman spectroscopy provides the capability to rapidly identify individual minerals because they have unique crystal lattices that produce distinct Raman spectra (band positions and shapes) (Nasdala et al. 2004). In addition to identification, compositional information can be quantitatively determined in solid solution systems of olivine, spinel, pyroxene, garnet, and feldspar by using the linear shift of mode frequency (Mernagh and Hoatson 1997; Kolesov and Geiger 1998; Huang et al. 2000; Wang et al. 2001; Nasdala et al. 2004; Smith 2005; Kuebler et al. 2006; Bendel and Schmidt 2008; Freeman et al. 2008; Bersani et al. 2009). Modes shift because solid solutions modify the lattice environment by shifting bond angles, lengths, and strengths. The lattice environment of feldspars is expected to be structurally similar, but the abundance of alkali cations and the degree of Si/Al ordering may shift modes.

Raman spectra can be used to distinguish distinct feldspar compositions (Freeman et al. 2008) and our recent calibrations allow feldspar compositions to be determined based on mode frequency. We examined the wavenumber position of modes common to the 9 analyzed feldspar compositions (Fig. 4). Freeman et al. (2008) demonstrate one example of linear correlation for the  $\nu_{22}$  mode, but our data only partially overlaps theirs (Fig. 4b). We identified one binary solution for all feldspar compositions using  $\nu_{25}$  (Fig. 4d). The linear relationship between Ab mol% and frequency includes all feldspar compositions. It has a slope of

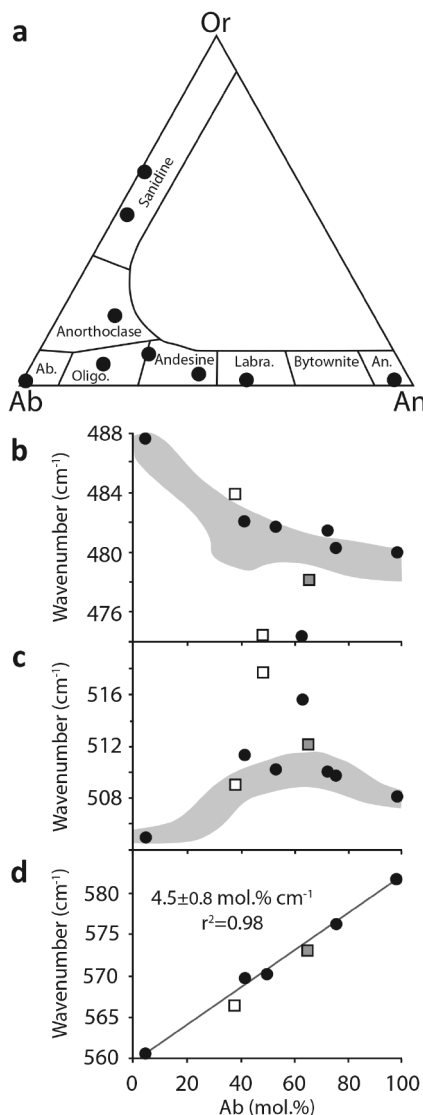


**FIGURE 4.** (a) Ternary plot of compositions of analyzed alkali and plagioclase feldspars. (b–d) Compositional dependence of mode frequency for three prominent modes. Data from Freeman et al. (2008) shown by gray domain when possible. Alkali feldspars are shown by squares (anorthoclase is gray; sanidine are white). Wavenumber and compositional uncertainties are less than symbol sizes.

$4.5 \pm 0.8 \text{ mol.\% cm}^{-1}$  and displays an  $r^2 = 0.98$ . We suggest that  $\nu_{25}$  may be the most determinative for feldspar compositions, but in the future this result should be substantiated by using a larger sample suite.

The  $\nu_{24}$  is one of the most intense modes in each sample. It does not correlate linearly with feldspar composition. Instead, frequency increases from Ab<sub>0</sub> to ~Ab<sub>75</sub>, and then frequency decreases approaching Ab<sub>100</sub> (Fig. 4b). Freeman et al. (2008) similarly document this nonlinear relationship between  $\nu_{24}$  and feldspar composition (they call mode  $\nu_{24}$  “Band I<sub>a</sub>”). Freeman et al. (2008) suggest that mode  $\nu_{24}$  forms clusters related to feldspar structure and composition, and that extracting a continuous

correlative relationship may not be appropriate. Our data align with their inference, but we question why  $\nu_{24}$  clusters but other modes in feldspars, and other silicates, produce linear and non-linear correlations. Mode  $\nu_{24}$  is produced by compression and expansion of the tetrahedral rings of Si, Al, and O, as well as by translation of Na along the a-axis (McKeown 2005). Compositional variations in Na thus could be expected to systematically modify the frequency of  $\nu_{24}$ . Isotope-dependent frequency shifts demonstrate that Na does not contribute to  $\nu_{24}$  frequency (Aliatis et al. 2015). Furthermore, isotope modeling also suggests that Si and Al content also do not contribute to  $\nu_{24}$ . If true, then  $\nu_{24}$  frequency shifts are not controlled by specific cation positions or abundances, and are instead related to lattice vibrations controlled by unidentified atomistic characteristics of feldspars.

### Raman frequency shift with pressure

Modes shift to higher wavenumbers with increasing pressure up to ~3.6 GPa (Fig. 3). The shift is caused by compression of the crystal lattice with increasing pressure. The rate of shift to higher wavenumber varies with mode and feldspar composition (Supplemental<sup>1</sup> Table 1). In an independent study, Aliatis et al. (2017) measured the pressure dependence of albite’s Raman spectra at pressures up to 10 GPa. They focused on 6 specific modes, and observed shifts to higher frequency with increasing pressure at rates of 1.1 to 3.6 cm<sup>-1</sup> GPa<sup>-1</sup>. They show shifts were linear at pressures up to ~6.5 GPa, indicating no change in the deformation mechanism of albite at crustal pressures. Our data set overlaps with some of their results as we measured the shift of the same albite bands incrementally at pressures up to ~3 GPa. Our calculated Raman shifts for those same modes differ by 5 to 50%. We suggest that our data sets largely agree, with discrepancies attributable to shift uncertainties (Supplemental<sup>1</sup> Table 1) and experimental design. Their data displays excellent linear trends above ~2 GPa, but have fewer data at lower pressures. We focused on low-pressure conditions, and thus have twice as many measurements and tighter control in the 0–3 GPa interval. Together, our data sets demonstrate that albite and other feldspars have linear shifts similar to other silicates, which have been experimentally determined to range from 1 to 4 cm<sup>-1</sup> GPa<sup>-1</sup> (e.g., rutile: Samara and Peercy 1973; Liu and Mernagh 1992; quartz: Hemley 1987; diamond: Tardieu et al. 1990; Al<sub>2</sub>SiO<sub>5</sub> polymorphs: Mernagh and Liu 1991; forsterite: Wang et al. 1993; magnetite: Shebanova and Lazor 2003; albite: Aliatis et al. 2017). Because mode frequencies are sensitive to the atomic environment of minerals, silicates should be expected to respond comparably as they are related by similar bonding, ions, and symmetry (Geiger and Kolesov 2002).

In all compositions in which they were identified, the ethanol modes  $\nu_{x2}$  and  $\nu_{x3}$ , display a parabolic relationship between frequency and pressure (Fig. 5). Wavenumber decreases from ambient pressures up to ~0.5 GPa, where the slope then reverses to produce a positive linear correlation similar to the linear shifts observed in all other modes. Although the trend is linear above 0.5 GPa, we did not provide the slope of the shift in Supplemental<sup>1</sup> Table 1 to emphasize this behavior.

### Raman mode separation and pressure

Modes  $\nu_{22}$  and  $\nu_{24}$  are prominent vibrations in all of the targeted feldspars. Those modes are always in close proximity, with

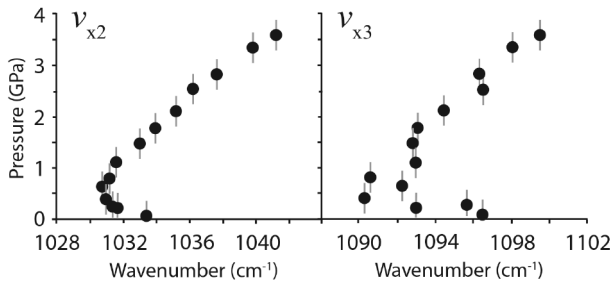


**FIGURE 5.** Modes  $\nu_{x2}$  and  $\nu_{x3}$  in ethanol display nonlinear, parabolic wavenumber shift with increasing pressure.

no other modes or noise separating them. In some instances,  $\nu_{22}$  occurs superimposed on the left shoulder of the larger  $\nu_{24}$ . The wavenumber distance between  $\nu_{22}$  and  $\nu_{24}$  provides an additional metric for characterizing the Raman signature of feldspars. We find an unreliable correlation between feldspar composition and band separation ( $r^2 \sim 0.5$ ). However, if feldspar composition is known a priori, pressure can be constrained using the band separation of those modes (with the exception of anorthite) (Fig. 6). The distance between the two becomes smaller with increasing pressure because  $\nu_{22}$  shifts to higher wavenumber faster than  $\nu_{24}$  by 1 to 2  $\text{cm}^{-1} \text{GPa}^{-1}$  (Supplemental Table 1). With increasing pressure,  $\nu_{22}$  must eventually overtake  $\nu_{24}$ . When sufficient pressures are attained the less intense  $\nu_{22}$  becomes unresolvable. We recognize the obfuscation of  $\nu_{22}$  in andesine at 3.5 GPa and in potassic sanidine at 1.6 GPa, but did not reach high enough pressures to obscure that mode in the other samples. Aliatis et al. (2017) showed that  $\nu_{22}$  becomes difficult to recognize in albite at pressures  $>8$  GPa. If  $\nu_{22}$  is not identified then the sample likely preserves high pressures because it is common to all feldspars at low pressure (Mernagh 1991; Freeman et al. 2008; Aliatis et al. 2015, 2017).

Albite, andesine, and oligoclase show particularly strong linear relationships between mode separation and pressure ( $r^2 > 0.98$ ) (Fig. 6). Those clear trends present an opportunity to confidently extract pressure from mode separation in many metamorphic and felsic magmatic systems. In addition, Raman thermobarometry is typically limited by the spectral resolution of the Raman system, which is rarely better than  $0.5 \text{ cm}^{-1}$ . This mode separation barometer requires much less sensitivity because the modes are separated by 20 to 30  $\text{cm}^{-1}$  at pressures up to 3 GPa. Thus, many workhorse Raman systems with spectral resolutions of 1–2  $\text{cm}^{-1}$  can be used to generate meaningful pressures.

### Feldspar Raman barometry

The crystal lattice of magmatic, metamorphic, and mantle minerals will relax as the sample ascends to ambient  $P$ - $T$  conditions. In some instances, a residual stress is preserved if the target mineral phase occurs as an inclusion within a crystal host. The crystal host acts as protective pressure vessel that preserves a residual pressure in the inclusion crystal.

The comparative elastic properties of both the inclusion and host phases provide the basis for inclusion barometry. Volume changes of host and inclusion during cooling and ascent are controlled by their respective expansivities and compressibilities

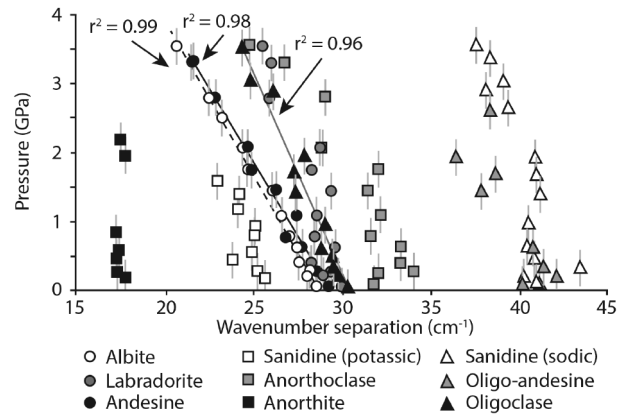


**FIGURE 6.** Frequency separation between  $\nu_{24}$  and  $\nu_{25}$ . Albite, andesine, and oligoclase display strong linear correlation (arrowed) between separation and pressure.

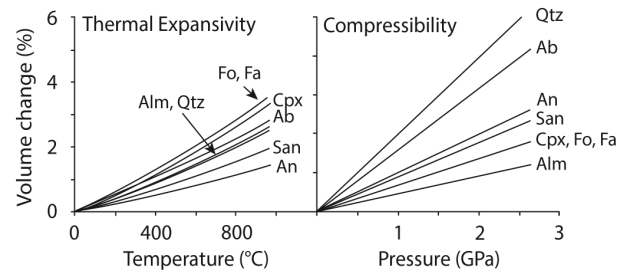


**FIGURE 7.** Comparison of thermal expansivity and compressibility of mineral phases (Berman 1988). Relative differences in thermal expansivity lead to potential thermometers, whereas relative differences in compressibility lead to barometers.

(Berman 1988; Holland and Powell 2011). Raman spectroscopy is used to establish the shift between the pressurized inclusion and the same phase at ambient conditions. A pressurized inclusion preserved within a protective host will produce the expected Raman modes, but they will be shifted to higher wavenumbers. The pressure of the inclusion can then be quantified if the pressure dependency of the shift is empirically known, as it now is for feldspars in light of our DAC experiments. Finally, entrapment conditions can be calculated using the elastic model in Equation 1, which depends on the relationship between phase volume, host shear modulus, and the temperature/pressure conditions (e.g., Guiraud and Powell 2006; Kohn 2014; Angel et al. 2017).

Feldspars have elastic properties that suggest they would make sensitive Raman barometers when they occur as crystal-line inclusions. We use the Berman (1988) thermodynamic database to establish our understanding of the elastic behavior of feldspars, which we then support with recent empirical results (Angel 2004; Benusa et al. 2005; Tribaudino et al. 2010, 2011). Bulk modulus measurements indicate that feldspars are softer than potential host phases like olivine, pyroxene, and garnet, but are harder than quartz. Bulk modulus increases from albite to anorthite, such that anorthite is 40% stiffer (Angel 2004; Brown et al. 2016). Bulk moduli results imply that feldspars

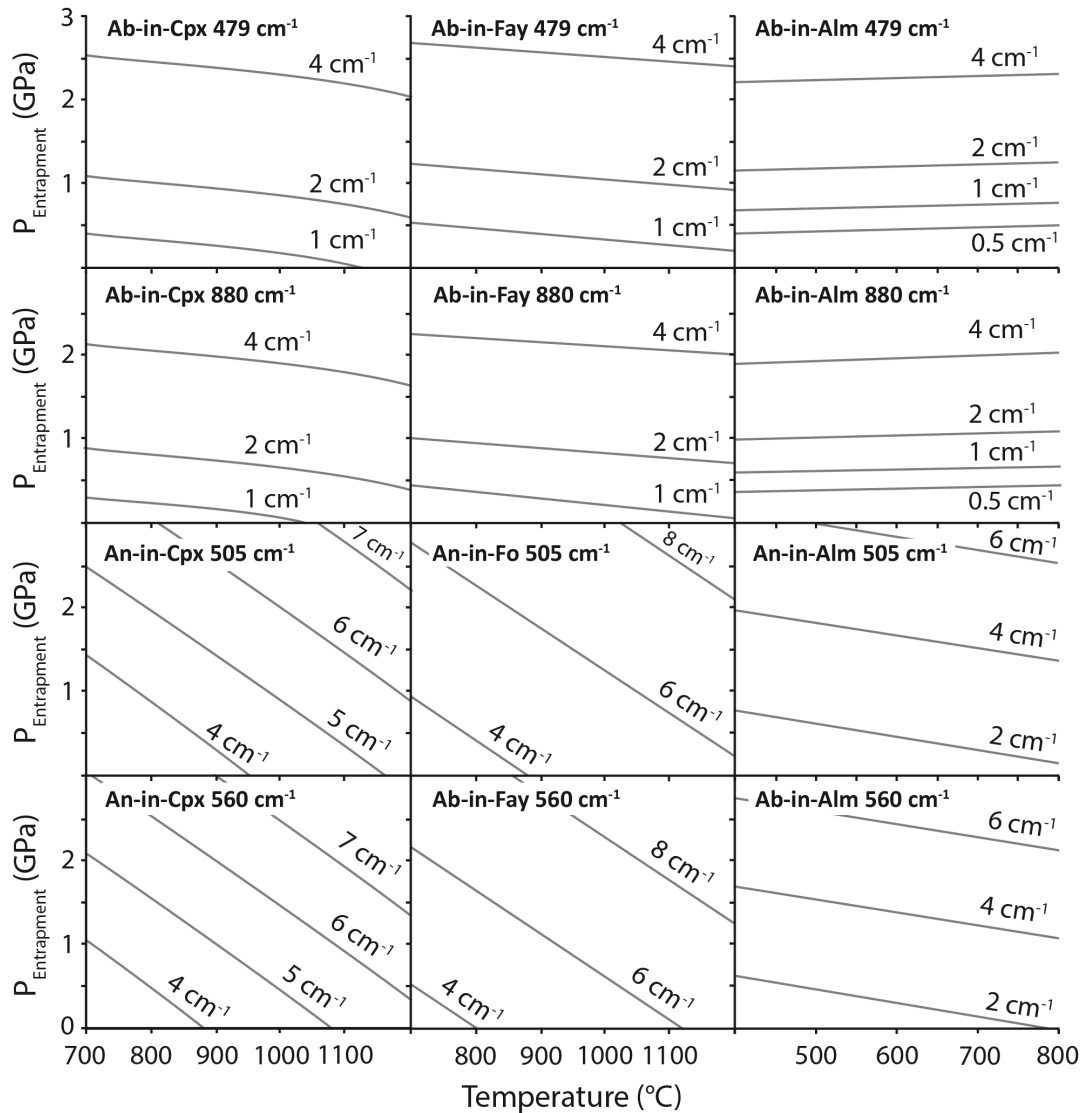


**FIGURE 8.** Entrapment  $P$ - $T$  conditions of feldspar inclusions in potential magmatic and metamorphic hosts. Inclusion pressures are given by Raman shift lines (labeled). Modes for the end-member feldspars are provided to demonstrate that numerous modes can be used to extract  $P$ - $T$  conditions, but the sensitivity of the individual modes vary. Calculations use Equation 1, thermodynamic variables from Berman (1988), and shear moduli of Cpx = 72.2 GPa (Collins and Brown 1998), Fa<sub>100</sub> = 51.2 GPa (Speziale et al. 2004), Alm = 92.1 GPa (Wang and Ji 2001), Fo<sub>93</sub> = 77.4 GPa (Liu et al. 2005).

will elastically respond to containment behavior, and that albite is the most sensitive composition. Feldspar thermal expansivity varies with composition following a curving trend. Albite has the highest thermal expansivity, which is nearly double that of anorthite (Tribaudino et al. 2010).

The effects of expansivity and compressibility counter one another during ascent from magmatic crystallization conditions. As magmas cool, crystals thermally contract, but they elastically expand as pressure decreases. Feldspar volume should decrease by 2–3% during cooling from magmatic temperatures, and expand by ~1% as it ascends from chamber depths (Fig. 7). Simultaneously, the host phase changes volume at different rates in response to its elastic properties. The relative difference in the elastic response between the feldspar inclusion and crystalline

host determines the effectiveness of Raman barometry. Barometers are marked by large differences in the compressibility of the inclusion and host (e.g., garnet-quartz from Ashley et al. 2014b). The host crystal rigidly squeezes the expansive feldspar inclusion. Thermometers have host crystals that shrink significantly during cooling and thus compress the less expansive inclusion (olivine-hosted inclusions). Other host-inclusion pairs fall between the end-members, which mitigates some of the utility of the system (e.g., Kohn 2014).

We solved the elastic model (Eq. 1) for inclusion-host pairs to produce  $P$ - $T$  diagrams that display the entrapment conditions based on the inclusion pressure (Raman band shift) (e.g., Guiraud and Powell 2006; Ashley et al. 2014b; Kohn 2014; Angel et al. 2017). Any Raman mode could be used for these

calculations, but the best modes will occur in all compositions, be intense at all pressures, have strong pressure sensitivity, and have sharp peaks that are easy to define. Using these criteria, we find that no single band provides a perfect combination of presence, sensitivity, intensity, and resolution. But, we identify five bands optimize those criteria and we suggest that the best modes for barometry are  $\nu_{14}$ ,  $\nu_{22}$ ,  $\nu_{24}$ , and  $\nu_{25}$ . Of those, mode  $\nu_{24}$  is the most intense at all pressures, making it easy to identify on spectra. Mode  $\nu_{22}$  has the highest Raman shift with increasing pressure (e.g., pressure-sensitive). Ab-rich plagioclase inclusions will be the most effective barometers in many hosts because mode shifts produce horizontal trends in  $P$ - $T$  space (Fig. 8), and Ab-rich plagioclase is most compressible. Alkali feldspars and An-rich plagioclase can also be used for barometry in many hosts, but their pressure sensitivity is less because of reduced compressibility. Raman shifts are generally  $<2 \text{ cm}^{-1}$  for upper lithospheric conditions.

Barometry applications are limited by the spectral resolution of available Raman systems. Currently available commercial Raman systems have maximum spectral resolutions of  $\sim 1 \text{ cm}^{-1}$ . Using those systems, feldspar barometry will be most effective for understanding relatively high-pressure environments including mafic magmas, mantle rocks, and mid-crustal metamorphic systems. Silica-rich magmas are stored in the shallow crust, and hence inclusions will not preserve resolvable shifts on low-resolution systems. High-resolution Raman systems with spectral resolutions of  $\sim 0.1 \text{ cm}^{-1}$  are present in some labs (e.g., Virginia Tech in Ashley et al. 2014a). Such high-resolution would have uncertainties  $<100 \text{ MPa}$  (1 kb), and allow effective thermobarometry for shallow magmatic systems and low-grade metamorphic rocks.

We find that olivine and clinopyroxene are distinctive host phases because of their relatively high thermal expansivity. Olivine- and clinopyroxene-hosted feldspar inclusions produce significant temperature sensitivity because lines of equal Raman shift are inclined (Fig. 8). In geologic environments where pressures can be realistically constrained to  $<300 \text{ MPa}$ , the shift is a thermometer. For example, anorthite inclusions in forsterite can constrain entrapment temperature within  $100 \text{ }^\circ\text{C}$  (Fig. 8). We recognize that such estimates have large uncertainties, but may be useful in settings that lack other reliable thermometry.

### IMPLICATIONS

We expand the application potential of Raman spectroscopy with our study of the pressure dependence of mode frequency in a suite of compositionally diverse feldspars. We also demonstrate that isobaric mode frequency may vary systematically with feldspar composition. Because feldspars are common minerals in the Earth's crust and rocky planetary bodies, Raman spectroscopy of feldspars can now be used to extract quantitative compositional and thermobarometric information in many new environments. Mobile Raman instruments installed on future space rovers can boldly go resolve feldspar composition, which will inform researchers on planetary magma evolution and differentiation (e.g., Wang et al. 1995, 2001; Freeman et al. 2008). Similarly, our calibration supplements existing databases that can be used with Raman to non-destructively establish provenance for feldspars in pottery and other archaeological materials (e.g., Nasdala et al. 2004).

Innovative thermobarometers are welcome tools for igneous and metamorphic petrologists. In recent years Raman thermobarometry calibrations have led to many fascinating constraints on mantle and metamorphic systems (e.g., Parkinson and Katayama 1999; Izraeli et al. 1999; Sobolev et al. 2000; Kohn 2014; Ashley et al. 2014a, 2015a, 2015b; Angel et al. 2015). Raman shifts of feldspar inclusions now provide an additional avenue for thermobarometry of magmas, in addition to metamorphic and mantle systems. Using the elastic properties of feldspar and common crystal hosts, we show that feldspar inclusions can be used to constrain pressure in mid-crustal to shallow mantle conditions. Those conditions include mafic magmas, medium- to high-grade metamorphic facies, and feldspar-bearing mantle environments. Shallower magmatic or metamorphic environments will not produce resolvable shifts. Accordingly, feldspar inclusions should not be informative about granite or rhyolite petrogenesis despite the abundance of feldspar in those rocks. Pressure-induced shifts in magmatic minerals including feldspar, olivine, quartz, and magnetite are now constrained, allowing many potential host-inclusion pairs relevant to thermobarometry in igneous rocks (Hemley 1987; Wang et al. 1993; Shebanova and Lazor 2003). Future studies must analyze feldspar inclusions in crystal hosts from diverse volcanic environments with well-known magmatic storage conditions. Such experiments will test our calculations and allow Raman feldspar thermobarometry to be extended later to unconstrained geologic systems.

### ACKNOWLEDGMENTS

We thank Smithsonian for feldspar samples NMNH 116398-15A and 88280-89. J.F.L. acknowledges support from the National Science Foundation Geophysics Program (EAR1446946). We also thank Mario Tribaudino and an anonymous reviewer for improving our manuscript.

### REFERENCES CITED

- Aliatis, I., Lambruschi, E., Mantovani, L., Bersani, D., Andò, S., Gatta, D., Gentile, P., Salvioli-Mariani, E., Prencipe, M., and Tribaudino, M. (2015) A comparison between ab initio calculated and measured Raman spectrum of triclinic albite ( $\text{NaAlSi}_3\text{O}_8$ ). *Journal of Raman Spectroscopy*, 46(5), 501–508.
- Aliatis, I., Lambruschi, E., Mantovani, L., Bersani, D., Gatta, G.D., Tribaudino, M., and Lottici, P.P. (2017) High-pressure Raman spectroscopy on low albite. *Physics and Chemistry of Minerals*, 44(3), 213–220.
- Angel, R.J. (1994) Feldspars at high pressure. In I. Parsons, Eds., *Feldspars and their Reactions*, NATO ASI Series (Series C: Mathematical and Physical Sciences), vol. 421, p. 271–312. Springer, Dordrecht.
- (2004) Equations of state of plagioclase feldspars. *Contributions to Mineralogy and Petrology*, 146(4), 506–512.
- Angel, R., Nimis, P., Mazzucchelli, M., Alvaro, M., and Nestola, F. (2015) How large are departures from lithostatic pressure? Constraints from host–inclusion elasticity. *Journal of Metamorphic Geology*, 33(8), 801–813.
- Angel, R.J., Mazzucchelli, M.L., Alvaro, M., and Nestola, F. (2017) EosFit-Pinc: A simple GUI for host-inclusion elastic thermobarometry. *American Mineralogist*, 102, 1957–1960. doi:10.2138/am-2017-6190.
- Ashley, K.T., Caddick, M.J., Steele-MacInnis, M.J., Bodnar, R.J., and Dragovic, B. (2014a) Geothermobarometric history of subduction recorded by quartz inclusions in garnet. *Geochemistry, Geophysics, Geosystems*, 15(2), 350–360.
- Ashley, K.T., Steele-MacInnis, and, M., Caddick, M.J. (2014b) QuIB Calc: A MATLAB® script for geobarometry based on Raman spectroscopy and elastic modeling of quartz inclusions in garnet. *Computers & Geosciences*, 66, 155–157.
- Ashley, K.T., Darling, R.S., Bodnar, R.J., and Law, R.D. (2015a) Significance of “stretched” mineral inclusions for reconstructing  $P$ - $T$  exhumation history. *Contributions to Mineralogy and Petrology*, 169(6), 1–9. doi:10.1007/s00410-015-1149-0.
- Ashley, K.T., Thigpen, J.R., and Law, R.D. (2015b) Prograde evolution of the Scottish Caledonides and tectonic implications. *Lithos*, 224, 160–178.
- Bendel, V., and Schmidt, B.C. (2008) Raman spectroscopic characterisation of disordered alkali feldspars along the join  $\text{KAlSi}_3\text{O}_8$ - $\text{NaAlSi}_3\text{O}_8$ : application to natural sanidine and anorthoclase. *European Journal of Mineralogy*, 20(6), 1055–1065.
- Benusa, M.D., Angel, R.J., and Ross, N.L. (2005) Compression of albite,  $\text{NaAlSi}_3\text{O}_8$ . *American Mineralogist*, 90(7), 1115–1120.

- Berman, R.G. (1988) Internally-consistent thermodynamic data for minerals in the system  $\text{Na}_2\text{O}-\text{K}_2\text{O}-\text{CaO}-\text{MgO}-\text{FeO}-\text{Fe}_2\text{O}_3-\text{Al}_2\text{O}_3-\text{SiO}_2-\text{TiO}_2-\text{H}_2\text{O}-\text{CO}_2$ . *Journal of Petrology*, 29(2), 445–522.
- Bersani, D., Andò, S., Vignola, P., Moltifiori, G., Marino, I.-G., Lottici, P.P., and Diella, V. (2009) Micro-Raman spectroscopy as a routine tool for garnet analysis. *Spectrochimica Acta Part A: Molecular and Biomolecular Spectroscopy*, 73(3), 484–491.
- Brown, J.M., Angel, R.J., and Ross N. (2016) Elasticity of plagioclase feldspars. *Journal of Geophysical Research*, 2, 663–675. doi:10.1002/2015JB012736.
- Collins, M.D., and Brown, J.M. (1998) Elasticity of an upper mantle clinopyroxene. *Physics and Chemistry of Minerals*, 26, 7–13.
- Daniel, I., Gillet, P., McMillan, P.F., Wolf, G., and Verhelst, M.A. (1997) High-pressure behavior of anorthite: Compression and amorphization. *Journal of Geophysical Research*, 102, 10,313–10,325.
- Deer, W.A., Howie, R.A., and Zussman, J., Eds. (2001) *Rock-Forming Minerals: Feldspars*, vol. 4A. Geological Society of London.
- Freeman, J.J., Wang, A., Kuebler, K.E., Jolliff, B.L., and Haskin, L.A. (2008) Characterization of natural feldspars by Raman spectroscopy for future planetary exploration. *Canadian Mineralogist*, 46(6), 1477–1500.
- Frogner, P., Broman, C., and Lindblom, S. (1998) Weathering detected by Raman spectroscopy using Al-ordering in albite. *Chemical Geology*, 151(1), 161–168.
- Gaetani, G.A., O'Leary, J.A., Shimizu, N., Bucholz, C.E., and Newville, M. (2012) Rapid reequilibration of  $\text{H}_2\text{O}$  and oxygen fugacity in olivine-hosted melt inclusions. *Geology*, 40(10), 915–918.
- Geiger, C.A., and Kolesov, B.A. (2002) Microscopic-macroscopic relationships in silicates: Examples from IR and Raman spectroscopy and heat capacity measurements. *EMU Notes in Mineralogy*, 4, 347–387.
- Guiraud, M., and Powell, R. (2006) P–V–T relationships and mineral equilibria in inclusions in minerals. *Earth and Planetary Science Letters*, 244(3), 683–694.
- Hemley R. (1987) Pressure dependence of raman spectra of  $\text{SiO}_2$  polymorphs:  $\alpha$ -quartz, coesite, and stishovite. *High-Pressure Research in Mineral Physics: a Volume in Honor of Syun-iti Akimoto*, 347–359.
- Holland, T.J.B. (1980) The reaction albite = jadeite + quartz determined experimentally in the range 600–1200 °C. *American Mineralogist*, 65(1-2), 129–134.
- Holland, T., and Powell, R. (2011) An improved and extended internally consistent thermodynamic dataset for phases of petrological interest, involving a new equation of state for solids. *Journal of Metamorphic Geology*, 29(3), 333–383.
- Huang, E., Chen, C., Huang, T., Lin, E., and Xu, J. (2000) Raman spectroscopic characteristics of Mg-Fe-Ca pyroxenes. *American Mineralogist*, 85(3-4), 473–479.
- Izraeli, E., Harris, J., and Navon, O. (1999) Raman barometry of diamond formation. *Earth and Planetary Science Letters*, 173(3), 351–360.
- Kohn, M.J. (2014) “Thermoba-Raman-try”: Calibration of spectroscopic barometers and thermometers for mineral inclusions. *Earth and Planetary Science Letters*, 388, 187–196.
- Kolesov, B., and Geiger, C. (1998) Raman spectra of silicate garnets. *Physics and Chemistry of Minerals*, 25(2), 142–151.
- Kuebler, K.E., Jolliff, B.L., Wang, A., and Haskin, L.A. (2006) Extracting olivine (Fo–Fa) compositions from Raman spectral peak positions. *Geochimica et Cosmochimica Acta*, 70(24), 6201–6222.
- Lin, J.F., Liu, J., Jacobs, C., and Prapakempa, V.B. (2012) Vibrational and elastic properties of ferromagnetite across the electronic spin-pairing transition of iron. *American Mineralogist*, 97, 583–591.
- Liu, L.-G., and Mernagh, T. (1992) Phase transitions and Raman spectra of anatase and rutile at high pressures and room temperature. *European Journal of Mineralogy*, 4(1), 45–52.
- Liu, W., Kung, J., and Li, B. (2005) Elasticity of San Carlos olivine to 8 GPa and 1073 K. *Geophysical Research Letters*, 32(16), L16301.
- Lowenstern, J.B. (1995) Applications of silicate-melt inclusions to the study of magmatic volatiles. *Magmas, Fluids, and Ore Deposits*, 23, 71–99. Mineralogical Society of Canada.
- Mammone, J.F., and Sharma, S.K. (1980) Raman spectra of methanol and ethanol at pressures up to 100 kbar. *Journal of Physics and Chemistry*, 84, 3130–3134.
- Mao, H.K., Xu, J.A., and Bell, P.M. (1986) Calibration of the ruby pressure gauge to 800 kbar under quasi-hydrostatic conditions. *Journal of Geophysical Research: Solid Earth*, 91(B5), 4673–4676.
- Matson, D.W., Sharma, S.K., and Philpotts, J.A. (1986) Raman spectra of some tectosilicates and of glasses along the orthoclase-anorthite and nepheline-anorthite joins. *American Mineralogist*, 71(5-6), 694–704.
- McKeown, D.A. (2005) Raman spectroscopy and vibrational analyses of albite: From 25 °C through the melting temperature. *American Mineralogist*, 90(10), 1506–1517.
- Mernagh, T. (1991) Use of the laser Raman microprobe for discrimination amongst feldspar minerals. *Journal of Raman Spectroscopy*, 22(8), 453–457.
- Mernagh, T., and Hoatson, D. (1997) Raman spectroscopic study of pyroxene structures from the Murni Murni layered intrusion, Western Australia. *Journal of Raman Spectroscopy*, 28(9), 647–658.
- Mernagh, T.P., and Liu, L.-g. (1991) Raman spectra from the  $\text{Al}_2\text{SiO}_5$  polymorphs at high pressures and room temperature. *Physics and Chemistry of Minerals*, 18(2), 126–130.
- Nasdale, L., Smith, D.C., Kaindl, R., and Ziemann, M.A. (2004) Raman spectroscopy: analytical perspectives in mineralogical research. *Spectroscopic Methods in Mineralogy*, 6, 281–343.
- Parkinson, C., and Katayama, I. (1999) Present-day ultrahigh-pressure conditions of coesite inclusions in zircon and garnet: Evidence from laser Raman microspectroscopy. *Geology*, 27(11), 979–982.
- Prawer, S., and Nemanich, R.J. (2004) Raman spectroscopy of diamond and doped diamond. *Philosophical Transactions of the Royal Society of London A: Mathematical, Physical and Engineering Sciences*, 362, 2537–2565.
- Rudnick, R.L., and Fountain, D.M. (1995) Nature and composition of the continental crust: a lower crustal perspective. *Reviews of Geophysics*, 33(3), 267–309.
- Samara, G., and Peery, P. (1973) Pressure and temperature dependence of the static dielectric constants and Raman spectra of  $\text{TiO}_2$  (rutile). *Physical Review B*, 7(3), 1131.
- Sharma, S.K., Simons, B., and Yoder, H. (1983) Raman study of anorthite, calcium Tschermak's pyroxene, and gehlenite in crystalline and glassy states. *American Mineralogist*, 68(11-12), 1113–1125.
- Shebanova, O.N., and Lazor, P. (2003) Vibrational modeling of the thermodynamic properties of magnetite ( $\text{Fe}_3\text{O}_4$ ) at high pressure from Raman spectroscopic study. *The Journal of Chemical Physics*, 119(12), 6100–6110.
- Smith, D.C. (2005) The RAMANITA® method for non-destructive and in situ semi-quantitative chemical analysis of mineral solid-solutions by multidimensional calibration of Raman wavenumber shifts. *Spectrochimica Acta Part A: Molecular and Biomolecular Spectroscopy*, 61(10), 2299–2314.
- Sobolev, N.V., Fursenko, B.A., Goryainov, S.V., Shu, J., Hemley, R.J., Mao, H., and Boyd, F.R. (2000) Fossilized high pressure from the Earth's deep interior: The coesite-in-diamond barometer. *Proceedings of the National Academy of Sciences*, 97(22), 11,875–11,879.
- Solin, S., and Ramdas, A. (1970) Raman spectrum of diamond. *Physical Review B*, 1(4), 1687.
- Speziale, S., Duffy, T.S., and Angel, R.J. (2004) Single-crystal elasticity of fayalite to 12 GPa. *Journal of Geophysical Research: Solid Earth*, 109 (B12), B12202.
- Tardieu, A., Cansell, F., and Petit, J. (1990) Pressure and temperature dependence of the first-order Raman mode of diamond. *Journal of Applied Physics*, 68(7), 3243–3245.
- Thomas, J.B., Watson, E.B., Spear, F.S., Shemella, P.T., Nayak, S.K., and Lanzirrotti, A. (2010) TitanQ under pressure: the effect of pressure and temperature on the solubility of Ti in quartz. *Contributions to Mineralogy and Petrology*, 160(5), 743–759.
- Tribaudo, M., Angel, R., Cámara, F., Nestola, F., Pasqual, D., and Margiolaki, I. (2010) Thermal expansion of plagioclase feldspars. *Contributions to Mineralogy and Petrology*, 160(6), 899–908.
- Tribaudo, M., Bruno, M., Nestola, F., Pasqual, D., and Angel, R.J. (2011) Thermodynamic and thermodynamic properties of plagioclase feldspars from thermal expansion measurements. *American Mineralogist*, 96(7), 992–1002.
- Velde, B., and Boyer, H. (1985) Raman microprobe spectra of naturally shocked microcline feldspars. *Journal of Geophysical Research*, 90(B5), 3675–3681.
- Wallace, P.J., Anderson, A.T., and Davis, A.M. (1999) Gradients in  $\text{H}_2\text{O}$ ,  $\text{CO}_2$ , and exsolved gas in a large-volume silicic magma system: Interpreting the record preserved in melt inclusions from the Bishop Tuff. *Journal of Geophysical Research: Solid Earth*, 104(B9), 20,097–20,122.
- Wang, Z., and Ji, S. (2001) Elasticity of six polycrystalline silicate garnets at pressure up to 3.0 GPa. *American Mineralogist*, 86(10), 1209–1218.
- Wang, S., Sharma, S., and Cooney, T. (1993) Micro-Raman and infrared spectral study of forsterite under high pressure. *American Mineralogist*, 78(5-6), 469–476.
- Wang, A., Jolliff, B.L., and Haskin, L.A. (1995) Raman spectroscopy as a method for mineral identification on lunar robotic exploration missions. *Journal of Geophysical Research*, 100, 21,189–21,199.
- Wang, A., Jolliff, B.L., Haskin, L.A., Kuebler, K.E., and Viskupic, K.M. (2001) Characterization and comparison of structural and compositional features of planetary quadrilateral pyroxenes by Raman spectroscopy. *American Mineralogist*, 86(7-8), 790–806.
- Waters, L.E., and Lange, R.A. (2015) An updated calibration of the plagioclase-liquid hygrometer-thermometer applicable to basalts through rhyolites. *American Mineralogist*, 100(10), 2172–2184.
- Watson, E.B., Wark, D.A., and Thomas, J.B. (2006) Crystallization thermometers for zircon and rutile. *Contributions to Mineralogy and Petrology*, 151, 413.
- Zhukov, V., and Korsakov, A. (2015) Evolution of host-inclusion systems: a viscoelastic model. *Journal of Metamorphic Geology*, 33, 815–828.

MANUSCRIPT RECEIVED APRIL 10, 2017

MANUSCRIPT ACCEPTED JANUARY 5, 2018

MANUSCRIPT HANDLED BY RENAT ALMEEV

## Endnote:

<sup>1</sup>Deposit item AM-18-46157, Supplemental Table. Deposit items are free to all readers and found on the MSA web site, via the specific issue's Table of Contents (go to [http://www.minsocam.org/MSA/AmMin/TOC/2018/Apr2018\\_data/Apr2018\\_data.html](http://www.minsocam.org/MSA/AmMin/TOC/2018/Apr2018_data/Apr2018_data.html)).